LUND UNIVERSITY

Reconstruction of equivalent currents using a near-field data transformation - with radome applications

Persson, Kristin; Gustafsson, Mats

2004

Link to publication

Citation for published version (APA):
Persson, K., & Gustafsson, M. (2004). *Reconstruction of equivalent currents using a near-field data transformation - with radome applications*. (Technical Report LUTEDX/(TEAT-7125)/1-15/(2004); Vol. TEAT-7125). [Publisher information missing].

Total number of authors:
2

General rights
Unless other specific re-use rights are stated the following general rights apply:
Copyright and moral rights for the publications made accessible in the public portal are retained by the authors and/or other copyright owners and it is a condition of accessing publications that users recognise and abide by the legal requirements associated with these rights.
• Users may download and print one copy of any publication from the public portal for the purpose of private study or research.
• You may not further distribute the material or use it for any profit-making activity or commercial gain
• You may freely distribute the URL identifying the publication in the public portal

Read more about Creative commons licenses: https://creativecommons.org/licenses/

Take down policy
If you believe that this document breaches copyright please contact us providing details, and we will remove access to the work immediately and investigate your claim.

LUND UNIVERSITY

PO Box 117
221 00 Lund
+46 46-222 00 00

CODEN:LUTEDX/(TEAT-7125)/1-15/(2004)

Reconstruction of Equivalent Currents using a Near-field Data Transformation—with Radome Applications

Kristin Persson and Mats Gustafsson

Department of Electroscience
Electromagnetic Theory
Lund Institute of Technology
Sweden

Kristin Persson and Mats Gustafsson

Department of Electroscience
Electromagnetic Theory
Lund Institute of Technology
P.O. Box 118
SE-221 00 Lund
Sweden

Editor: Gerhard Kristensson
© Kristin Persson and Mats Gustafsson, Lund, June 17, 2004

Abstract

Knowledge of the current distribution on a radome can be used to improve radome design, detect manufacturing errors, and to verify numerical simulations. In this paper, the transformation from near-field data to its equivalent current distribution on a surface, *i.e.*, the radome, is analyzed. The transformation is based on the surface integral representation that relates the equivalent currents to the near-field data. The presence of axial symmetry enables usage of the fast Fourier transform (FFT) to reduce the computational complexity. Furthermore, the problem is regularized using the singular value decomposition (SVD). Both synthetic and measured data are used to verify the method. The quantity of data is vast since the height of the radome corresponds to $29 - 43$ wavelengths in the frequency interval $8.0 - 12.0$ GHz. It is shown that the method gives an accurate description of the field radiated from an antenna, on a surface enclosing it. Moreover, defects on the radome, not localized in the measured near field, are focused and detectable on the radome surface.

1 Introduction

There are several applications of a near field to equivalent currents transformation. For example, in the radome industry it is important to have accurate models of the field from the antenna inside the radome. This field cannot be measured directly since the radome often is placed very close to the antenna and at these distances, there is a substantial interaction between the antenna and the measuring probe [3, 7, 12]. Another field of application is in the manufacturing of radiating bodies, *i.e.*, radomes, antenna arrays *etc.*, when the radiation pattern from the body does not exhibit the expected form. By determination of the equivalent currents on the radiating body the malfunctioning areas or components can be found.

A common method, transforming near field to equivalent currents and vice versa, is to use modal-expansions of the electric field [3]. This is a very efficient method for radiating bodies with certain geometrical symmetries, *i.e.*, spherical and cylindrical. The radial solutions contain cylindrical and spherical Bessel functions while the angular solutions are described by trigonometric functions and the associated Legendre functions, respectively [3, 11]. For general geometrical symmetries, where modal-expansions do not exist, the method is not applicable.

In this paper, another approach utilizing the surface integral representation is derived from the Maxwell equations and then inverted, *i.e.*, a linear inverse source problem is solved. By this method it is possible to handle a wider class of geometries [7, 8]. The surface integral representation provides a relation relating the unknown electric and magnetic equivalent currents on a surface to the measured electric field. An additional relation is given by the fact that the equivalent currents are constructed such that the integral is zero inside the volume, on which surface the currents exist, *i.e.*, the extinction theorem [10].

The integral relations are discretized into matrix linear equations. The matrix equations include an azimuthal convolution which is solved with a fast Fourier trans-

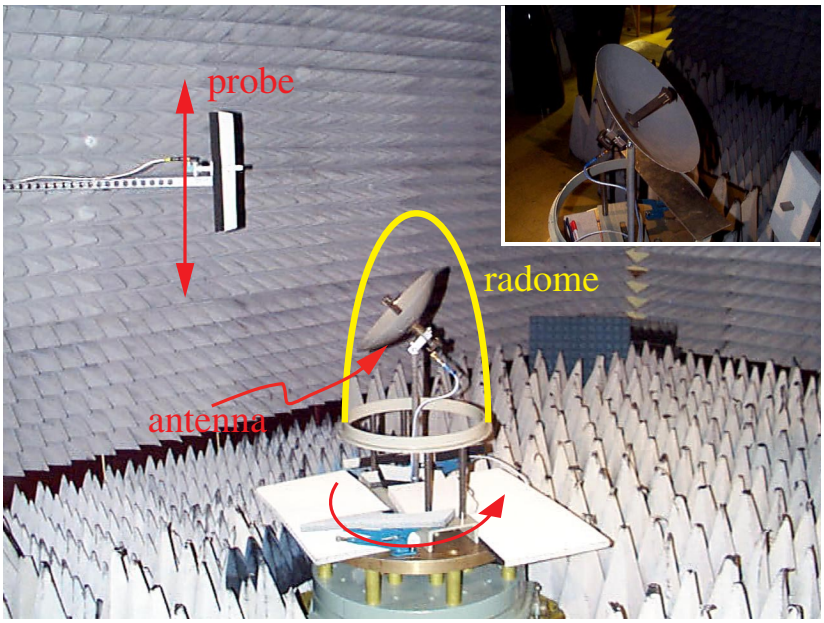

Figure 1: Photo of the cylindrical near-field range at SAAB Bofors Dynamics, Sweden. The antenna under test is rotated and the probe is moved in the vertical direction. A close up of the reflector antenna is shown in the upper right corner.

form (FFT) in the angular coordinate. The fast Fourier transform brings down the complexity of the problem, *i.e.*, the original surface-to-surface linear map is decomposed into a set of line-to-line linear maps. A singular value decomposition (SVD) is used to invert each of these linear maps. As most inverse problems it is ill-posed, *i.e.*, small errors in the near-field data can produce large errors in the equivalent currents. Thus, the problem needs to be regularized by suppression of small singular values when inverted.

In this paper, the electric field to be inverted is presumed to be scalar. The assumption is acceptable since the used near-field data, supplied by SAAB Bofors Dynamics and Chelton Applied Composites, Sweden, clearly have one dominating component. The measured data is given for three different antenna and radome configurations, *viz.*, antenna, antenna together with radome, and antenna together with defect radome. The height of the radome corresponds to $29 - 43$ wavelengths in the frequency interval $8.0 - 12.0$ GHz.

As a start, synthetic data is used to verify the method. Verification is also performed by a comparison between the measured far field and the far field calculated from the equivalent currents on the radome. The calculated far field agrees well with the measured far field. We show that the method describes the field radiated from an antenna, on a surface enclosing it, in a correct way. When the radome is introduced the field is scattered and flash lobes arise. The equivalent currents on the radome, that produce the electric field measured in the near-field area, are identified and the flash lobes are accurately detected.

Manufacturing errors, not localized in the measured near-field data, can be fo-

cused and detected on the radome surface. In this paper, it is shown that the field scattered by copper plates attached on the radome, are focused back towards the original position of the copper plates. The length of the side of the square copper plates is 6 cm, *i.e.*, $1.6 - 2.4$ wavelengths corresponding to the frequency span $8.0 - 12.0$ GHz.

In Section 2 the experimental set-up is described and the measured near-field data is presented. The surface integral representation is introduced and adapted to the specific problem in Section 3. Section 4 discusses the implementation process of the surface integral representation. Some adjustments of the formulas are performed and the error of the method is elucidated. The results, when using the experimental near-field data, are shown and examined in Section 5. The paper ends with the achieved conclusions in Section 6.

2 Near-field Measurements

The near-field data, used in this paper, was supplied by SAAB Bofors Dynamics and Chelton Applied Composites, Sweden. The set-up with relevant dimensions indicated is shown in Figures 1 and 2. Three different measurements were performed; data measured without the radome, data measured with the radome, and data measured with the defect radome. The defect radome has two copper plates attached to its surface.

A reflector antenna fed by a symmetrically placed wave-guide generates the near-field data, see Figure 1. The diameter of the antenna is 0.32 m and its focal distance is 0.1 m. The main lobe of the antenna is vertically polarized relative to the horizontal plane. The standing wave ratio (SWR) is approximately 1.4 in the frequency range $8.2 - 9.5$ GHz. The antenna is poorly adapted for other frequencies. A 10 dB reflection attenuator is connected to the antenna.

The radome surface is described by

$$\rho(z) = \begin{cases} 0.213\,\mathrm{m} & -0.728\,\mathrm{m} \leq z \leq -0.663\,\mathrm{m} \\ -(bz' + d) + \sqrt{(bz' + d)^2 - a(z')^2 - 2cz' - e} & -0.663\,\mathrm{m} < z \leq 0.342\,\mathrm{m} \end{cases}$$

where $z' = z + 0.728\,\mathrm{m}$ and the constants are $a = 0.122$, $b = 0.048$, $c = -0.018\,\mathrm{m}$, $d = 0.148\,\mathrm{m}$, and $e = -0.108\,\mathrm{m}^2$. The near-field measurement probe consists of a wave-guide for which no compensation is made in the final data. The cylindrical surface, where the electric field is measured, is placed in both the reactive near-field zone and the radiating near-field zone [2, Chap 2].

The amplitude and phase of the electric field are measured in the frequency interval $8.0 - 12.0$ GHz on a cylindrical surface by moving the probe in the z-direction and rotating the antenna under test, see Figure 1. In angle, 120 points are measured between $-180°$ and $180°$ in steps of $3°$. The z-dimension is divided into 129 points, every two points separated by 12.5 mm. This means that at 8.0 GHz the electric field is measured 3 times per wavelength, in the z-direction, and 1.5 times per wavelength, in the angular direction, respectively. Together, a total of $120 \times 129 = 15480$ measurement points are used for each radome configuration and frequency. The co-

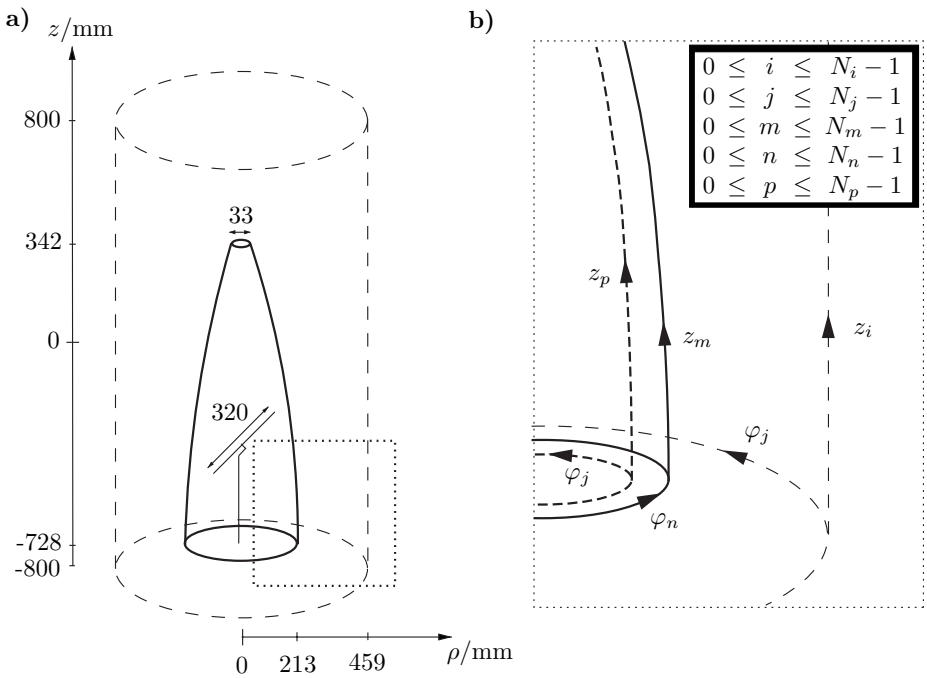

Figure 2: (a) The dimensions of the reflector antenna, the radome, and the cylinder where the electric near field is measured. (b) A close-up showing the discretized geometric variables.

and cross-polarized measured electric fields are shown in Figure 3. The differences between the three different antenna and radome cases arise from constructive and destructive interference between the radiated field and the scattered field. In Figure 3 it is also observed that the electric field consists of a dominating co-component, *i.e.*, a dominating z-component since the antenna is vertically polarized, in the forward direction.

3 The Surface Integral Representation

The surface integral representation expresses the electromagnetic field in a homogeneous and isotropic region in terms of its values on the bounding surface. The representation states that if the electromagnetic field on a surface of a volume is known, the electromagnetic field in the volume can be determined [5, 10]. The representation is derived starting from the time harmonic Maxwell equations with the time convention $\mathrm{e}^{\mathrm{i}\omega t}$. The Maxwell equations transform into the vector Helmholtz equation

$$\nabla^2 \boldsymbol{E}(\boldsymbol{r}) + k^2 \boldsymbol{E}(\boldsymbol{r}) = 0 \tag{3.1}$$

since the material (air) is source free, homogeneous, and isotropic.

Assume that the electric field consists only of a component in the z-direction, *i.e.*, the equations are scalar. This is a good approximation dealing with the specific

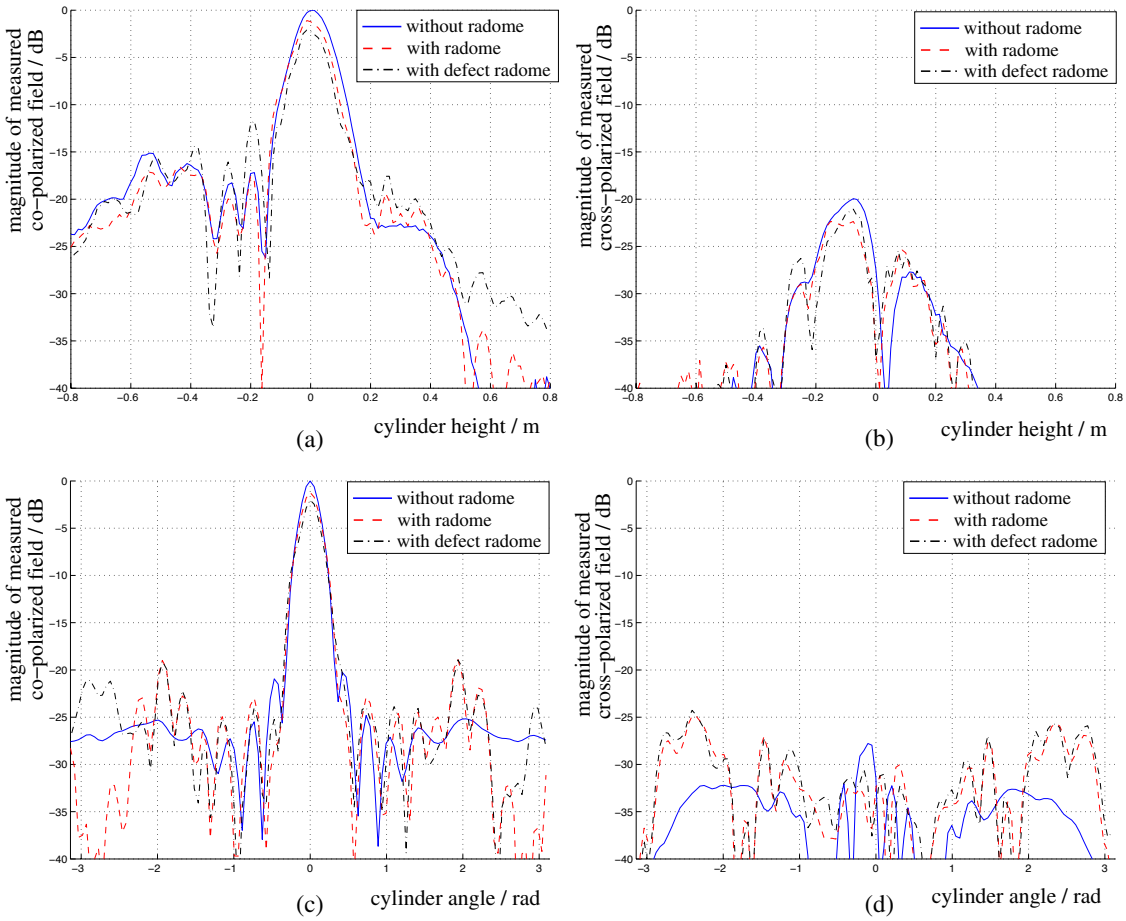

Figure 3: The measured co- and cross-polarized electric field on the measurement cylinder at 8.0 GHz. In (a) and (b) the angle is fixed at $\varphi = 0$, and the fields are normalized to the maximum value when no radome is present in (a). In (c) and (d) the height is fixed at $z = 0$, and the fields are normalized to the maximum value when no radome is present in (c).

measurements described in Section 2, where the z-component is clearly the dominating one, *cf.* Figure 3, and the prime interest is to reconstruct the electric field in the main lobe.

Working with a scalar field, the surface integral representation only depends on the scalar electric field, E_z, and its normal derivative, $\frac{\partial E_z}{\partial n}$, *i.e.*, the magnetic field is not taken into account as it must in the full three dimensional expression [5]. The scalar surface integral representation is derived using the Green's function $g(\boldsymbol{r}, \boldsymbol{r}') = \frac{\mathrm{e}^{-\mathrm{i}k|\boldsymbol{r}-\boldsymbol{r}'|}}{4\pi|\boldsymbol{r}-\boldsymbol{r}'|}$ of the problem [10]

$$\iint_S \left[\frac{\partial g(\boldsymbol{r}, \boldsymbol{r}')}{\partial n} E_z(\boldsymbol{r}) - g(\boldsymbol{r}, \boldsymbol{r}') \frac{\partial E_z(\boldsymbol{r})}{\partial n} \right] \mathrm{d}S = \begin{cases} -E_z(\boldsymbol{r}') & \boldsymbol{r}' \in V \\ 0 & \boldsymbol{r}' \notin V \end{cases} \tag{3.2}$$

where V is the volume spanning from the outside of the radome to infinity. The

closed surface S is the radome surface with an added top and bottom surface. Observe that the electric field does not have to be zero outside the volume, *i.e.*, inside the radome. The surface integral representation (3.2) only states that the left-hand side of the equation is zero if the vector $\boldsymbol{r}'$ points outside the volume V, *i.e.*, the extinction theorem [10].

The equivalent surface currents are introduced as

$$M(\boldsymbol{r}) \equiv E_z(\boldsymbol{r}) \quad \text{and} \quad M'(\boldsymbol{r}) \equiv \frac{\partial E_z(\boldsymbol{r})}{\partial n} \tag{3.3}$$

which are inserted in (3.2) to give

$$\iint_S \left[\frac{\partial g(\boldsymbol{r},\boldsymbol{r}')}{\partial n} M(\boldsymbol{r}) - g(\boldsymbol{r},\boldsymbol{r}')M'(\boldsymbol{r})\right] \mathrm{d}S = \begin{cases} -E_z^{\mathrm{cyl}}(\boldsymbol{r}') & \boldsymbol{r}' \in \text{cylinder} \\ 0 & \boldsymbol{r}' \in \text{surface inside radome} \end{cases} \tag{3.4}$$

where E_z^{cyl} is the z-component of the electric field on the measurement cylinder. The continuous variables are discretized to give linear matrix equations. The discretized cylindrical coordinate system is described by the integer indices displayed in Figure 2.

3.1 Angular Fourier Transformation

The transformation (the Green's function) is axially symmetric due to the measurement set-up, see Section 2. Observe that the symmetry only applies to the transformation, not to the electric field. Thus, the left-hand side in (3.4) represents a convolution and by using a Fourier transformation of the angle coordinate the computational complexity can be brought down one dimension. This reduction of one dimension, can be understood by writing the left-hand side in (3.4) as a matrix X. This matrix is a circulant matrix, *i.e.*, every row is shifted one step to the right compared to the previous row. The eigenvectors of all circulant matrices are the column vectors of the Fourier matrix F. When a circulant matrix is multiplied with the Fourier matrix. *i.e.*, performing the Fourier transformation, the result is $FX = F\Lambda$ where Λ is a diagonal matrix, which can be seen as a reduction of one dimension [9, Chap 4.2].

Discretization and Fourier transformation, in the angle coordinate, of (3.4) give

$$\sum_{m=0}^{N_m-1} \left[\widehat{\mathcal{G}}'_{im\hat{\jmath}}\widehat{M}_{m\hat{\jmath}} \; - \widehat{\mathcal{G}}_{im\hat{\jmath}}\widehat{M}'_{m\hat{\jmath}}\right] = -\widehat{E}^{\mathrm{cyl}}_{i\hat{\jmath}} \qquad \text{for all } \; i, \hat{\jmath} \tag{3.5}$$

and

$$\sum_{m=0}^{N_m-1} \left[\widehat{\mathsf{G}}'_{pm\hat{\jmath}}\widehat{M}_{m\hat{\jmath}} \; - \widehat{\mathsf{G}}_{pm\hat{\jmath}}\widehat{M}'_{m\hat{\jmath}}\right] = 0 \qquad \text{for all } \; p, \hat{\jmath} \tag{3.6}$$

where $\mathcal{G}$ and G are the surface integrals, taken over the radome, of the Green's function multiplied with the basis functions used in the discretization process. $\mathcal{G}$ has the discretized space variable $\boldsymbol{r}'$ belonging to the measurement cylinder and

G has the discretized space variable $\boldsymbol{r}'$ belonging to a surface inside the radome, respectively. The prime denotes the normal derivative of the Green's function, $\hat{\jmath}$ is the integer index belonging to the Fourier transformed angle component, and the "hat" denotes the Fourier transformed variables. The summation limits N_m and N_p are described in Figure 2. To solve the surface integral representation, a limit process of equation (3.6) should be performed by forcing the fictitious surface inside the radome towards the radome surface [2,6]. However, in our attempt to find a simple and feasible method to allocate the surface current the use of the extinction theorem as an approximate solution to the integral representation in equation (3.6) is sufficient.

Reduction of M' in (3.5) and (3.6) gives

$$\sum_{m=0}^{N_m-1}\left\{\widehat{\mathcal{G}}'_{im\hat{\jmath}}-\sum_{p=0}^{N_p-1}\sum_{q=0}^{N_m-1}\widehat{\mathcal{G}}_{iq\hat{\jmath}}\,(\widehat{\mathsf{G}}^{-1})_{qp\hat{\jmath}}\,\widehat{\mathsf{G}}'_{pm\hat{\jmath}}\right\}\widehat{M}_{m\hat{\jmath}}\;=-\widehat{E}^{\mathrm{cyl}}_{i\hat{\jmath}}\qquad\text{for all }\;i,\hat{\jmath}\tag{3.7}$$

Equation (3.7) can also be written as $\hat{\jmath}$ matrix equations

$$\widehat{\boldsymbol{G}}^{\mathrm{radome}}_{\hat{\jmath}}\,\widehat{\boldsymbol{M}}_{\hat{\jmath}}\;=-\widehat{\boldsymbol{E}}^{\mathrm{cyl}}_{\hat{\jmath}}\qquad\text{for all }\;\hat{\jmath}\tag{3.8}$$

where the matrices are defined as $\widehat{\boldsymbol{M}}_{\hat{\jmath}}\equiv[\widehat{M}_{m1}]_{\hat{\jmath}}$, $\widehat{\boldsymbol{E}}^{\mathrm{cyl}}_{\hat{\jmath}}\equiv[\widehat{E}^{\mathrm{cyl}}_{i1}]_{\hat{\jmath}}$, and

$$\widehat{\boldsymbol{G}}^{\mathrm{radome}}_{\hat{\jmath}}\equiv[\widehat{\mathcal{G}}'_{im}]_{\hat{\jmath}}-[\widehat{\mathcal{G}}_{im}]_{\hat{\jmath}}[\widehat{\mathsf{G}}_{mp}]^{-1}_{\hat{\jmath}}[\widehat{\mathsf{G}}'_{pm}]_{\hat{\jmath}}\tag{3.9}$$

The notation of matrices used here is that of [1].

3.2 Inversion with Singular Value Decomposition

Since the matrices $\widehat{\boldsymbol{G}}^{\mathrm{radome}}_{\hat{\jmath}}$ and $[\widehat{\mathsf{G}}_{mp}]_{\hat{\jmath}}$ in (3.8) and (3.9) are not quadratic, a regular inversion cannot be performed. A fast and easy way to solve this is to use the singular value decomposition (SVD) [9, Chap 1.6]. This method is used on both matrices, but the SVD-equations are only given here for $\widehat{\boldsymbol{G}}^{\mathrm{radome}}_{\hat{\jmath}}$. The matrix system (3.8) can then be rewritten as

$$\widehat{\boldsymbol{U}}_{\hat{\jmath}}\widehat{\boldsymbol{S}}_{\hat{\jmath}}\widehat{\boldsymbol{V}}^{\dagger}_{\hat{\jmath}}\widehat{\boldsymbol{M}}_{\hat{\jmath}}=-\widehat{\boldsymbol{E}}^{\mathrm{cyl}}_{\hat{\jmath}}\qquad\text{for all }\;\hat{\jmath}\tag{3.10}$$

where $\widehat{\boldsymbol{V}}^{\dagger}_{\hat{\jmath}}$ denotes the Hermitian conjugate of $\widehat{\boldsymbol{V}}_{\hat{\jmath}}$. Both $\widehat{\boldsymbol{U}}_{\hat{\jmath}}$ and $\widehat{\boldsymbol{V}}_{\hat{\jmath}}$ are orthogonal matrices. $\widehat{\boldsymbol{S}}_{\hat{\jmath}}$ is a diagonal matrix consisting of the singular values to $\widehat{\boldsymbol{G}}^{\mathrm{radome}}_{\hat{\jmath}}$ in decreasing order. The singular values of both $\widehat{\boldsymbol{G}}^{\mathrm{radome}}_{\hat{\jmath}}$ and $[\widehat{\mathsf{G}}_{mp}]_{\hat{\jmath}}$ exhibit the tendency shown by the curves in Figure 4. The curves all reach down to $-300\,\mathrm{dB}$, *i.e.*, the calculation accuracy of MATLAB, where they level out.

A cut-off value δ normalized to the operator L_2-norm of $\widehat{\boldsymbol{G}}^{\mathrm{radome}}_{1}$ is chosen. The operator L_2-norm of $\widehat{\boldsymbol{G}}^{\mathrm{radome}}_{1}$ is equal to the largest singular value (σ_1) of the largest Fourier transformed angle component [6, Chap 15]. All singular values smaller than

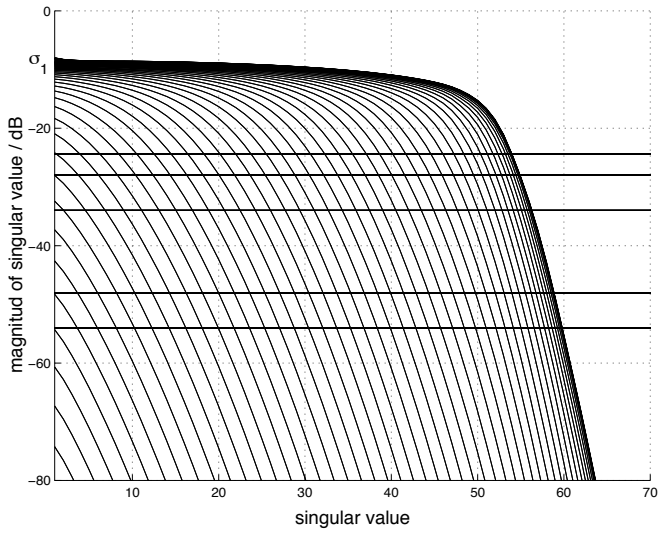

Figure 4: The tendency of singular values of $\widehat{\boldsymbol{G}}_{\hat{\jmath}}^{\text{radome}}$ and $[\widehat{\mathsf{G}}_{mp}]_{\hat{\jmath}}$. Every curve represents the singular values of a Fourier transformed angle component, *i.e.*, different $\hat{\jmath}$. The horizontal lines describe the cut-off values $\delta = \sigma_1[0.15\ 0.1\ 0.05\ 0.01\ 0.005]$.

δ are ignored during the inversion of $\widehat{\boldsymbol{S}}_{\hat{\jmath}}$ and are afterwards set to zero. If this is not done the small singular values create an uncontrolled growth of non-radiation currents when inverted. The mathematical formulation then fails since very small electric field contributions become dominating. Performing the inversion of (3.10) gives

$$\widehat{\boldsymbol{M}}_{\hat{\jmath}} = -\,\widehat{\boldsymbol{U}}_{\hat{\jmath}}^{\dagger}\widehat{\boldsymbol{S}}_{\hat{\jmath}}^{-1}\widehat{\boldsymbol{V}}_{\hat{\jmath}}\widehat{\boldsymbol{E}}_{\hat{\jmath}}^{\text{cyl}} \qquad \text{for all } \hat{\jmath} \tag{3.11}$$

Before the system of equations is solved it is necessary to convert it back from Fourier space by an inverse Fourier transformation

$$\boldsymbol{M}_j = \mathcal{F}^{-1}\left[-\widehat{\boldsymbol{U}}_{\hat{\jmath}}^{\dagger}\widehat{\boldsymbol{S}}_{\hat{\jmath}}^{-1}\widehat{\boldsymbol{V}}_{\hat{\jmath}}\widehat{\boldsymbol{E}}_{\hat{\jmath}}^{\text{cyl}}\right] \qquad \text{for all } j, \hat{\jmath} \tag{3.12}$$

where j, as before, denotes the integer index belonging to the discretized angle component, see Figure 2.

4 Implementation

The software MATLAB is used to implement the mathematical formulas in Section 3. All the calculations are performed with approximately 16 significant digits. One of the major computational problems in the implementation process is due to the storage of the matrix $\widehat{\boldsymbol{G}}$, *cf*. (3.9). This matrix has approximately 10^8 elements at the frequency 8.0 GHz and a sample density of 10 points per wavelength both in the angular direction and in the z-direction on the radome.

Some adjustments of the formulas are made in the implementation process. To facilitate the calculations, the radome surface is reshaped into a closed surface by

adding a smooth top and bottom surface. These extra surfaces are useful since the measurements are performed under non-ideal conditions. The table, on which the antenna and radome are placed, see Figure 1, reflects some of the radiation, which is taken care of by the bottom surface. The top surface represents the electric field that is reflected on the inside of the radome and then is passed out through the top hole. If these factors are not considered, unwanted edge effects occur since the electric field originating from the table and the top of the radome is forced to arise from the radome itself.

The measured electric near field is only measured 1.5 times per wavelength, in the angular direction, at the frequency 8.0 GHz, see Section 2. To be sure that the equivalent currents on the radome are recreated in an accurate way it is necessary to have a high sample density on the radome, preferable 10 to 20 points per wavelength. This is achieved by increasing the number of discrete points, in the angular direction, on the radome surface by including extra angles between the already existing ones. Thus, the axial symmetry of the Green's transformation is kept. The sample density on the measurement cylinder contributes very little to the total error. The surface integral representation creates currents on the radome such that the electric field is correct at the measurement points. However, if the Nyquist theorem is fulfilled, then the electric field is correct at all points on the measurement surface, *i.e.*, not only at the measurement points.

To verify and find the error of the method, synthetic data is used. The error as a function of the Fourier transformed angle component is defined as

$$\begin{aligned} \mathrm{Err}(\hat{\jmath}) &= 20\log_{10}\frac{\|\widehat{\boldsymbol{M}}_{\hat{\jmath}} - \widehat{\boldsymbol{M}}_{\hat{\jmath}}^{\mathrm{correct}}\|_2}{\|\widehat{\boldsymbol{M}}_{\hat{\jmath}}^{\mathrm{correct}}\|_2} = \\ &= 20\log_{10}\frac{\sqrt{\sum_{m=0}^{N_m-1}|\widehat{M}_{m\hat{\jmath}} - \widehat{M}_{m\hat{\jmath}}^{\mathrm{correct}}|^2\Delta S_m}}{\sqrt{\sum_{m=0}^{N_m-1}|\widehat{M}_{m\hat{\jmath}}^{\mathrm{correct}}|^2\Delta S_m}} \qquad \text{for all } \hat{\jmath} \end{aligned} \tag{4.1}$$

where the matrix definition in (3.8) is used and ΔS_m denotes the discretized area elements on the radome.

By using synthetic data and choosing appropriate cut-off values δ the error is shown to be below -60 dB for each existing Fourier transformed angle component. To obtain these low error levels, the measurement surface must be closed, *i.e.*, field values at the top and bottom surfaces of the cylindrical measurement surface must be included. The cut-off values depend on the complexity of the specific measurement set-up and must be investigated for each new set-up.

The total error of the scalar surface integral representation using the measured near field described in Section 2 is hard to define since the noise level and the amount of field spread outside the measurement cylinder are unknown parameters. Instead we rely on the fact that the method handles synthetic data well and that the results using measured data is satisfactory, see Section 5.

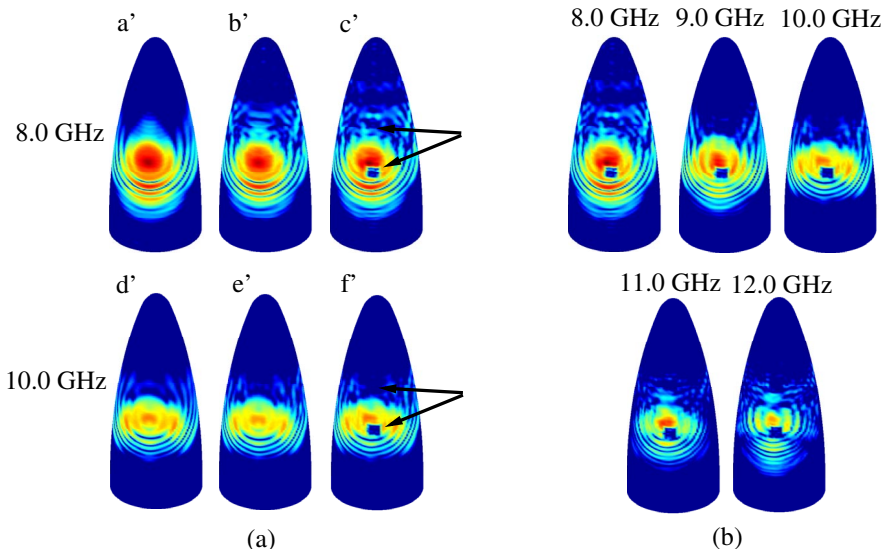

Figure 5: The reconstructed currents in dB-scale $[-30, 0]$, all normalized to the highest current value, *i.e.*, the maximum current magnitude in figure ac'. (a) The different measurement configurations are depicted at two different frequencies. From left to right; antenna without radome, antenna together with radome, and antenna together with defect radome, respectively. The arrows point out the location of the copper plates on the defect radome. (b) The defect radome case, shown at different frequencies.

5 Results using Measured Near-field Data

The measured near-field data, described in Section 2, is investigated. The inner fictitious surface is located one wavelength from the radome surface. The sample density on the radome is 10 points per wavelength both in the angular direction and in the z-direction. The cut-off values are determined in accordance with the discussion in Section 4.

Three different measurement configurations are investigated, *viz.*, antenna, antenna together with radome, and antenna together with defect radome. The studied frequency interval is $8.0 - 12.0\,\text{GHz}$. The results for the different measurement configurations are shown in Figure 5a at the frequencies 8.0 GHz and 10.0 GHz. In Figure 5b the results for the defect radome case are shown for the frequencies 8.0 GHz, 9.0 GHz, 10.0 GHz, 11.0 GHz, and 12.0 GHz, respectively.

In the case when no radome is placed around the antenna the equivalent currents are calculated on a surface shaped as the radome, see Figure 5aa' and 5ad'. The figures show that the near field close to the antenna is complex and hard to predict, *i.e.*, the diffraction pattern must be taken into account. The diffraction is explained as environmental reflections and an off-centered antenna feed.

The case when the radome is present, see Figure 5ab' and 5ae', shows in comparison to the case without radome that the used radome interacts with the antenna

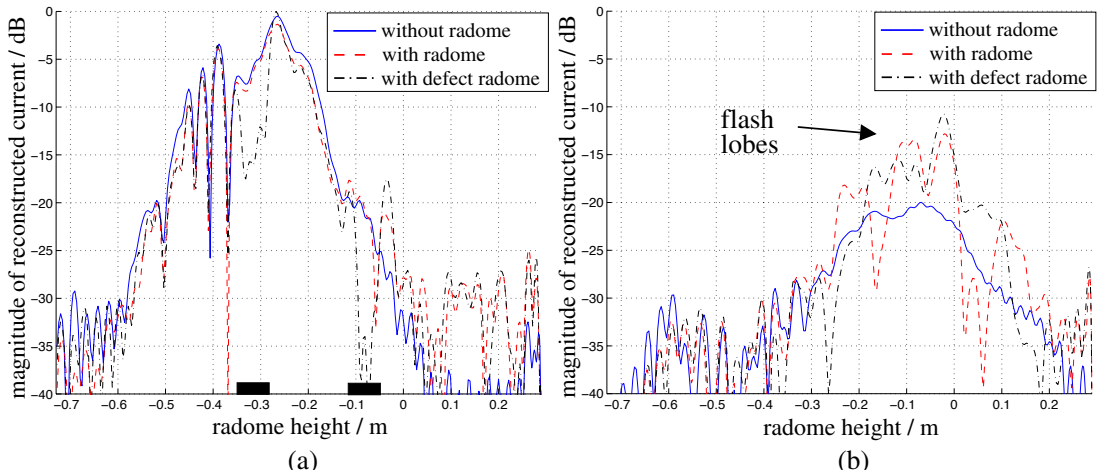

Figure 6: Cross section of the reconstructed currents on the radome surface for the different measurement configurations, at 8.0 GHz. The currents are shown as functions of the radome height for a fixed angle. All graphs are normalized to the highest current value, *i.e.*, the maximum current for the defect radome. (a) The graph representing the currents in the main lobe, *i.e.*, the front of the radome. The position of the copper plates are marked as thick lines on the horizontal axis. (b) The currents on the back of the radome.

and hence disturbs the radiated field. However, the currents in the main lobe are hardly affected by the radome, as seen in Figure 6a. The influence of the radome is clearly visible in the reconstructed currents on the back of the radome where flash lobes occur, see Figure 6b.

The defect radome has two copper plates attached to its surface. These are placed in the forward direction of main lobe of the antenna and centered at the heights 41.5 cm and 65.5 cm above the bottom of the radome. The length of the side of the squared copper plates is 6 cm, which corresponds to 1.6 wavelengths at 8.0 GHz and 2.4 wavelengths at 12.0 GHz, respectively. The locations of the copper plates are detected as shown in Figure 5ac' and 5af', where the lower plate appears clearly. The other plate is harder to discern since it is placed in a region with small current magnitudes. However, a cross section graph through the main lobe detects even this copper plate, see Figure 6a. Observe that the copper plates cannot be localized directly in the near-field data, compare Figure 6a to Figure 3a. The near-field data only shows that the field is disturbed, not the location of the disturbance. Nevertheless, by using the surface integral representation the plates are localized and focused. The defect radome also increases the backscattering as seen in Figure 6b. Due to the copper plates the flash lobes are different compared to the case with the non-defect radome.

As a final verification, the far-field amplitude on a sphere in the far-field region is studied. The electric field, originating from the equivalent currents on the radome,

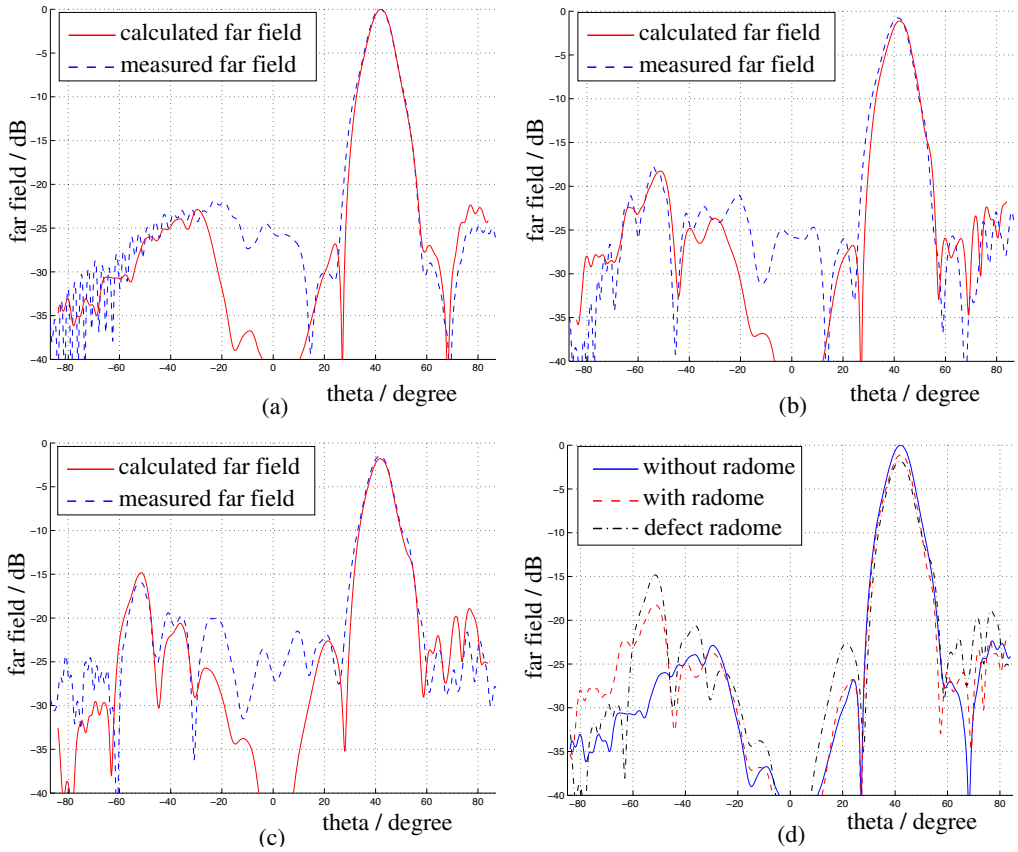

Figure 7: Comparison between the measured far-field data, supplied by Chelton Applied Composites, and the far field calculated from the equivalent currents on the radome surface. The far fields are normalized to the maximum value of the far field when no radome is present. (a) Antenna without radome. (b) Antenna together with radome. (c) Antenna together with defect radome. (d) The calculated far-field pattern for the three measurement configurations.

is calculated on the sphere,

$$\boldsymbol{E}_j^{\text{sph}} = -\mathcal{F}^{-1}\left[\widehat{\boldsymbol{G}}_{\hat{\jmath}}\widehat{\boldsymbol{M}}_{\hat{\jmath}}\right] \qquad \text{for all } j, \hat{\jmath} \tag{5.1}$$

in accordance with (3.8) and (3.12), except that $\widehat{\boldsymbol{G}}_{\hat{\jmath}}$ now describes the transformation from the radome to the inner fictitious surface and the far field sphere, respectively. The denotions j and $\hat{\jmath}$ are, as before, the integer index belonging to the discretized angle component and the Fourier transformed discretized angle component, respectively.

The far-field amplitude F is derived as

$$F(\theta, \phi) = kr\, \mathrm{e}^{\mathrm{i}kr} E^{\text{sph}}(r, \theta, \phi) \qquad \text{as } r \to \infty \tag{5.2}$$

where (r, θ, ϕ) describes the spherical coordinate system [4, Chap 10]. The result is compared with far-field data, supplied by Chelton Applied Composites, as shown in

Figure 7. The far field is depicted for the angles $\phi = 0$ and $\phi = \pi$, *i.e.*, a cross-section through the far field of the main lobe and the corresponding far field originating from the currents on the back of the radome. There is a lack of agreement between the measured far field and the calculated one in the angles corresponding to the top of the radome,*i.e.*, $\theta \approx 0$. This is due to the fact that fields originating hereof are not included in the measured near-field data used in the calculations, since the measurement surface is a cylinder. The fact that the radome disturbs and reflects the electric field, as earlier seen in Figure 6b, can also be detected in the far field, see Figure 7d, where flash lobes appear when the radome is present.

6 Discussion and Conclusions

The used scalar surface integral representation gives a linear map between the equivalent currents and the near-field data for general structures. It is shown that this map can be inverted for axially symmetric geometries. The model can theoretically be adapted to geometries lacking symmetry axes. Although it is not a feasible approach for radome applications, demanding large quantities of measured data, with the present computer capacity.

The transformation method is stable and useful in radome design and for evaluation purposes. To investigate the electric field passing through the radome, the current distribution on the antenna or on a surface enclosing the antenna must be known. Using the surface integral representation, the equivalent currents, on a surface enclosing the antenna, are described correctly.

Another range of application within the radome industry is to study how *e.g.*, lightning conductors and Pitot tubes, often placed on radomes, influence the equivalent currents. We show that such influences and the field effects of the radome itself are accurately detected. In this paper, copper plates are attached on the radome, in the direction of the antenna main lobe. The length of the side of the square copper plates are $1.6 - 2.4$ wavelengths, corresponding to the frequency span $8.0 - 12.0$ GHz. The plates cannot be localized directly using the near-field data, but by using the equivalent currents the effect of the copper plates are focused and detected on the radome surface. Thus, by transforming the near-field data to the radome surface, field defects introduced by the radome and other disturbances are focused back to their origins.

It is concluded that the transformation method based on the surface integral representation works very well and that the field of applications is large. A natural continuation is to elaborate the algorithm by including near field data with cross-polarization, *i.e.*, to implement the full Maxwell equations with a Method of Moments (MoM). Nevertheless, if the measured near-field data consists of one dominating component the use of the full Maxwell equations are not necessary, as shown in this paper.

Additional aspects to be investigated more thoroughly in the future are the resolution possibilities of manufacturing errors and other external field influences. Analysis of how the phase information in the near field can be used during the

transformation, is also to be analyzed further.

Acknowledgments

The work reported in this paper is sponsored by Försvarets Materielverk (FMV), Sweden, which is gratefully acknowledged.

The authors also like to express their gratitude to the people at SAAB Bofors Dynamics, Sweden, and especially to Michael Andersson and Sören Poulsen at Chelton Applied Composites, Sweden, for supplying the near-field data and pictures of the experimental setup.

References

[1] H. Anton. *Elementary Linear Algebra.* John Wiley & Sons, New York, 7 edition, 1994.

[2] C. A. Balanis. *Antenna Theory.* John Wiley & Sons, New York, second edition, 1997.

[3] J. E. Hansen, editor. *Spherical Near-Field Antenna Measurements.* Number 26 in IEE electromagnetic waves series. Peter Peregrinus Ltd., Stevenage, UK, 1988. ISBN: 0-86341-110-X.

[4] J. D. Jackson. *Classical Electrodynamics.* John Wiley & Sons, New York, second edition, 1975.

[5] D. S. Jones. *Acoustic and Electromagnetic Waves.* Oxford University Press, New York, 1986.

[6] R. Kress. *Linear Integral Equations.* Springer-Verlag, Berlin Heidelberg, 1999.

[7] Y. Rahmat-Samii, L. I. Williams, and R. G. Yaccarino. The UCLA bi-polar planar-near-field antenna-measurement and diagnostics range. *IEEE Antennas and Propagation Magazine*, **37**(6), 16–35, December 1995.

[8] T. K. Sarkar and A. Taaghol. Near-field to near/far-field transformation for arbitrary near-field geometry utilizing an equivalent electric current and MoM. *IEEE Trans. Antennas Propagat.*, **47**(3), 566–573, March 1999.

[9] G. Strang. *Introduction to applied mathematics.* Wellesley-Cambridge Press, Box 157, Wellesley MA 02181, 1986.

[10] S. Ström. Introduction to integral representations and integral equations for time-harmonic acoustic, electromagnetic and elastodynamic wave fields. In V. V. Varadan, A. Lakhtakia, and V. K. Varadan, editors, *Field Representations and Introduction to Scattering*, Acoustic, Electromagnetic and Elastic Wave Scattering, chapter 2, pages 37–141. Elsevier Science Publishers, Amsterdam, 1991.

[11] V. V. Varadan, Y. Ma, V. K. Varadan, and A. Lakhtakia. Scattering of waves by spheres and cylinders. In V. V. Varadan, A. Lakhtakia, and V. K. Varadan, editors, *Field Representations and Introduction to Scattering*, Acoustic, Electromagnetic and Elastic Wave Scattering, chapter 4, pages 211–324. Elsevier Science Publishers, Amsterdam, 1991.

[12] A. D. Yaghjian. An overview of near-field antenna measurements. *IEEE Trans. Antennas Propagat.*, **34**(1), 30–45, January 1986.